A comparison of lattice-Boltzmann and Brownian-dynamics simulations of polymer migration in confined flows

Rahul Kekre, Jason E. Butler, and Anthony J. C. Ladd

Department of Chemical Engineering, University of Florida,

Gainesville, Florida 32611-6005, USA

(Dated: June 14, 2010)

Abstract

This paper compares results from lattice-Boltzmann and Brownian-dynamics simulations of polymer migration in confined flows bounded by planar walls. We have considered both a uniform shear rate and a constant pressure gradient. Lattice-Boltzmann simulations of the center-of-mass distribution agree quantitatively with Brownian-dynamics results, contradicting previously published results. The mean end-to-end distance of the extended polymer is more sensitive to grid resolution, Δx, and time-step, Δt. Nevertheless, for sufficiently small Δx and Δt, convergent results for the polymer stretch are obtained which agree with Brownian-dynamics within statistical uncertainties. The Brownian dynamics simulations incorporate a mobility matrix for a confined polymer that is both symmetric and positive-definite for all physically accessible configurations.

I. INTRODUCTION

The lattice-Boltzmann (LB) method is one of a number of mesoscale simulation methods being developed to study the dynamics of complex fluids [1]. In contrast to particle-based methods such as Dissipative Particle Dynamics [2] or Multi-Particle Collision Dynamics [3], the fluid information is stored on a regular grid, simplifying the computation in a parallel programming environment. In common with other methods that include the fluid degrees of freedom explicitly, lattice-Boltzmann simulations are very flexible [1] and can include Brownian motion via thermally-driven fluctuations applied directly to the fluid [4]. Polymer solutions are modeled by coupling the polymer to an LB fluid with a frictional drag force [5]; this method has been applied to confined polymers as well [6]. It is important to ensure that LB simulations model the same physics as Brownian dynamics and two recent papers have investigated the relaxation of individual chains [7, 8]. Here we extend this work to flows of polymer solutions in a channel bounded by planar walls.

Numerical simulations [6, 9–11] of confined polymers driven by rectilinear flows have established the essential role of hydrodynamic interactions (HI) in polymer migration. The local shear rate extends the polymer and generates tension in the chain which disturbs the surrounding flow-field. In the vicinity of a boundary, this disturbance flow becomes asymmetric and produces a hydrodynamic lift of the polymer away from the wall. Migration in uniform shear [12] and pressure-driven flows [13] has been simulated by lattice-Boltzmann [6] and Brownian-dynamics [9], but quantitative comparisons between the two methods have not been made yet. On the other hand, static and dynamic properties of an isolated polymer calculated by LB and BD do agree, to within $1-2\%$ [7, 8]. The relaxation times of the internal degrees of freedom also match over the entire spectrum, showing that the hydrodynamic interactions are identical at both large and small length scales.

This paper reports quantitative comparisons between LB and BD simulations of a confined polymer chain driven by an external flow. Steady state distributions of the center of mass of the polymer and its end-to-end vector are found to be in quantitative agreement for both uniform shear and pressure-driven flows. These results are at variance with a previous study [14] in which the two methods predicted qualitatively different migration profiles in a pressure-driven flow. In that study, LB simulations of the polymer concentration did not capture the characteristic double peak observed in pressure-driven flow and showed signifi-

cantly less migration than BD simulations at a similar Weissenberg number (see Fig. 4 in Ref. [14]).

The BD simulations in this work use a regularized version [15] of the Green's function for a point force confined between two parallel plates [16]. The regularization accounts for the additional disturbance in the flow-field due to the finite-size of the source and receiver; it generates a symmetric and positive-definite mobility matrix for all physically relevant configurations of the polymer.

II. SIMULATION TECHNIQUES

A. Polymer Model

The polymer consists of $N+1$ beads of radius a with FENE springs connecting the neighboring beads;

$$\Phi_s = \sum_{i=1}^{N} \phi_s(|\boldsymbol{r}_i - \boldsymbol{r}_{i-1}|), \quad \phi_s(r) = -\frac{1}{2}\kappa r_0^2 \ln\left(1 - \frac{r^2}{r_0^2}\right), \tag{1}$$

where κ is the spring constant, r_0 is the maximum extension of the spring, and $\boldsymbol{r}_i$ is the position vector of the i^{th} bead. The simulations use a value of $r_0 = 5b$, where $b = \sqrt{T/\kappa}$ and T is the thermal energy corresponding to an absolute temperature T/k_B.

In addition to the FENE potential, there is an excluded volume interaction between the beads

$$\Phi_{ev} = \sum_{i>j} \phi_{ev}(|\boldsymbol{r}_i - \boldsymbol{r}_j|), \quad \phi_{ev}(r) = A\exp(-\beta r^2), \tag{2}$$

with $\beta = 1.80b^{-2}$ and $A = 2.70T$. The potential parameters in Eqs. (1) and (2) represent a coarse-grained approximation to a DNA molecule with 10 Kuhn segments per spring [17, 18]. We use $N = 10$ to model a DNA molecule with contour length $L_C = 10.6\ \mu m$. The equilibrium radius of gyration and end-to-end distance are $\langle R_G^2\rangle^{1/2} = 2.624b$ and $\langle R_E^2\rangle^{1/2} = 6.344b$ respectively.

The beads also experience a short range repulsion with a nearby wall, based on the loss of configurational entropy of an ideal chain,

$$\Phi_w = \sum_{i=0}^{N} \phi_w(y_i), \quad \phi_w(y) = T\left[E_1(-2\beta y^2/3) - E_1(-2\beta(H-y)^2/3)\right], \tag{3}$$

where y_i is the distance of center of the i^{th} bead from the lower wall, H is the separation between the walls, and $E_1(x)$ is the exponential integral function, $\int_x^\infty \frac{e^{-t}}{t} dt$. The total conservative force, $\boldsymbol{F}_i^C$, acting on the i^{th} bead is $-\nabla_{\boldsymbol{r}_i}(\Phi_s + \Phi_{ev} + \Phi_w)$. The polymer model described by Eqs. (1) - (3) is used in both the LB and BD simulations.

B. Lattice-Boltzmann

The lattice-Boltzmann method is implemented as described in Ref. [7] with the addition of the link bounce-back rule [4] to describe the no-slip condition at stationary or moving walls located at $y = 0$ and $y = H$. Periodic boundary conditions are applied in the x and z directions with a repeat length of L. To compare with Brownian dynamics, where the system is unconfined in directions parallel to the walls, we require $L \gg H$. However, the hydrodynamic interactions are exponentially screened by the no-slip boundaries [16] and $L > 2H$ has been found to be sufficient to approximate a single polymer bounded between parallel plates [6]. In this work we used a range of values $2 \leq L/H \leq 4$ to eliminate artifacts from the periodic boundary conditions.

The key parameters characterizing an inertial simulation of a shear flow are the Peclet or Weissenberg number ($\approx \gamma R_G^2/D$) and the Reynolds number ($\approx \gamma R_G^2/\nu$). The radius of gyration of the polymer, R_G, is the characteristic length, D is the polymer diffusivity, and γ is the shear rate. A large Peclet number can be achieved while keeping the Reynolds number small if the ratio $Sc = \nu/D$ is sufficiently large. In previous work on globular polymers [7] we found no evidence of inertial effects if the Schmidt number was larger than $40 - 50$. In order to allow for hydrodynamic interactions to develop between segments of chains that are extended by the flow, we here use larger Schmidt numbers, from $Sc \approx 300$ to $Sc \approx 2500$.

Single chain properties are insensitive to the mass of the bead, the fluid viscosity, and the interpolation method; the role of these parameters in a confined geometry was found to be negligible. The crucial parameters in obtaining accurate results for the dynamic properties are the grid-resolution, Δx, and the effective time step, Δt. We used $\Delta x = 2b$ and $\Delta x = 1.33b$, corresponding to a root-mean-square bond length $\langle r^2 \rangle^{1/2} \approx 0.87\Delta x$ and $\langle r^2 \rangle^{1/2} \approx 1.30\Delta x$. The effective time-step is based on the monomer diffusion time, $\Delta t = b^2/D_0$, and is controlled by the temperature of the LB fluid via the diffusion coefficient $D_0 = T/(6\pi\eta a)$. The hydrodynamic radius $a = 0.36b$ is chosen to match reported values for

DNA [17].

C. Brownian Dynamics

The Brownian-dynamics algorithm for a polymer chain in free space is summarized in Ref. [7]. Usually in such simulations, a regularized Green's function is used to ensure that the mobility matrix remains positive-definite. Here, we describe an implementation of a regularized and symmetric mobility matrix for particles confined between two parallel no-slip boundaries, with the geometry illustrated in Fig. 1.

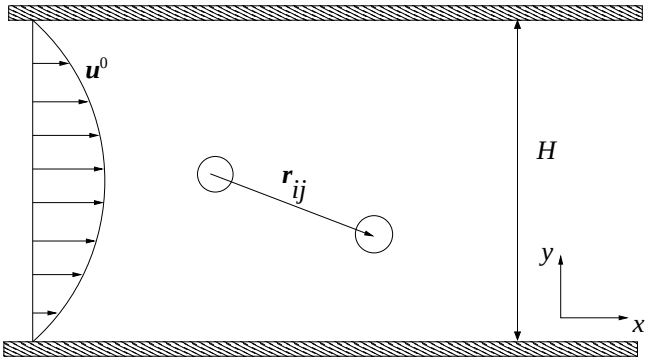

FIG. 1: Illustration of the configuration of beads i and j between two parallel plates.

The flow-field between two parallel plates due to a point force $\boldsymbol{F}$ is

$$\boldsymbol{u}(\boldsymbol{r}) = \boldsymbol{G}(\boldsymbol{r}, \boldsymbol{r}'|H) \cdot \boldsymbol{F}(\boldsymbol{r}'), \tag{4}$$

where H is the separation between the plates and $\boldsymbol{G}(\boldsymbol{r}, \boldsymbol{r}'|H)$ is the Green's function [16]. This Green's function can be decomposed into the free-space Green's function, $\boldsymbol{G}^{\infty}(\boldsymbol{r} - \boldsymbol{r}')$, corrections due to a planar boundary, $\boldsymbol{G}^{W}(\boldsymbol{r}, \boldsymbol{r}'; Y)$ [19] (Y is the location of the wall), and corrections due to multiple reflections between the boundaries $\boldsymbol{G}^{R}(\boldsymbol{r}, \boldsymbol{r}'|H)$,

$$\boldsymbol{G}(\boldsymbol{r}, \boldsymbol{r}'|H) = \boldsymbol{G}^{\infty}(\boldsymbol{r} - \boldsymbol{r}') + \boldsymbol{G}^{W}(\boldsymbol{r}, \boldsymbol{r}'; 0) + \boldsymbol{G}^{W}(\boldsymbol{r}, \boldsymbol{r}'; H) + \boldsymbol{G}^{R}(\boldsymbol{r}, \boldsymbol{r}'|H). \tag{5}$$

The pair mobility matrix is a regularization of this Green's function due to the finite size of the particles. The translational velocity $\boldsymbol{u}_i$ of the i^{th} bead (Fig. 1) due to the forces acting on the beads is

$$\boldsymbol{u}_i = \boldsymbol{u}_i^0 + \frac{\boldsymbol{F}_i}{6\pi\eta a} + \sum_{j \neq i} [\mathcal{L}_i \mathcal{L}_j \boldsymbol{G}(\boldsymbol{r}_i, \boldsymbol{r}_j|H)] \cdot \boldsymbol{F}_j, \tag{6}$$

where $\boldsymbol{u}_i^0$ is the unperturbed fluid velocity and the Faxen operator is

$$\mathcal{L}_i = \left(1 + \frac{a^2}{6}\nabla^2_{\boldsymbol{r}_i}\right). \tag{7}$$

In the region $|r_{ij}| \geq 2a$, the operators $\mathcal{L}_i$ and $\mathcal{L}_j$, acting on the Oseen tensor, $\boldsymbol{G}^\infty(\boldsymbol{r}_j - \boldsymbol{r}_i)$, generate the far-field part of the Rotne-Prager (RP) interaction [20]. The RP tensor including the near-field values of $\boldsymbol{r}_{ij} = \boldsymbol{r}_j - \boldsymbol{r}_i$ is

$$\boldsymbol{\mu}_{ij}^{RP} = \frac{1}{6\pi\eta a}\begin{cases} C_1\boldsymbol{I} + C_2\dfrac{\boldsymbol{r}_{ij}\boldsymbol{r}_{ij}}{r_{ij}^2} & r_{ij} \geq 2a \\ C_1'\boldsymbol{I} + C_2'\dfrac{\boldsymbol{r}_{ij}\boldsymbol{r}_{ij}}{r_{ij}^2}, & r_{ij} < 2a \\ 1, & i = j, \end{cases} \tag{8}$$

where the constants are

$$\begin{aligned} C_1 &= \frac{3}{4}\frac{a}{r_{ij}} + \frac{1}{2}\frac{a^3}{r_{ij}^3}, \quad C_2 = \frac{3}{4}\frac{a}{r_{ij}} - \frac{3}{2}\frac{a^3}{r_{ij}^3}, \\ C_1' &= 1 - \frac{9}{32}\frac{r_{ij}}{a}, \qquad C_2' = \frac{3}{32}\frac{r_{ij}}{a}. \end{aligned} \tag{9}$$

Thus, the mobility matrix of a pair of confined particles is

$$\boldsymbol{\mu}_{ij} = \boldsymbol{\mu}_{ij}^{RP} + \mathcal{L}_i\mathcal{L}_j\left[\boldsymbol{G}^W(\boldsymbol{r}_i, \boldsymbol{r}_j; 0) + \boldsymbol{G}^W(\boldsymbol{r}_i, \boldsymbol{r}_j; H) + \boldsymbol{G}^R(\boldsymbol{r}_i, \boldsymbol{r}_j|H)\right]. \tag{10}$$

The stiff repulsive potential between the beads and the wall, Eq. (3), removes the need for a specific short-range function for the HI with the wall.

Expressions for the regularized Green's function for a single wall, $\mathcal{L}_i\mathcal{L}_j\boldsymbol{G}^W(\boldsymbol{r}_i, \boldsymbol{r}_j; Y)$, are given in Ref. [15]. The contribution from higher reflections, $\mathcal{L}_i\mathcal{L}_j\boldsymbol{G}^R$, is calculated by numerically applying the Faxen operators to the reflection term $\boldsymbol{G}^R$, isolated from the Liron-Mochon solution, Eq. (4), for point particles. Explicit expressions for $\boldsymbol{G}^R$ are available in the literature [21, 22].

The computation time for $\mathcal{L}_i\mathcal{L}_j\boldsymbol{G}^R$ is several orders of magnitude larger than the superposed mobility matrix,

$$\boldsymbol{\mu}_{ij}^{S} = \boldsymbol{\mu}_{ij}^{RP} + \mathcal{L}_i\mathcal{L}_j\left[\boldsymbol{G}^W(\boldsymbol{r}_i, \boldsymbol{r}_j; 0) + \boldsymbol{G}^W(\boldsymbol{r}_i, \boldsymbol{r}_j; H)\right]. \tag{11}$$

Therefore the superposed solution, which contains all the singular contributions [21], is computed at each time step, while contributions from the multiple reflections are interpolated from a precalculated table. The details of the look-up table are described in Appendix A.

The interpolated Green's function is not divergence free. Therefore, the Langevin equation describing the motion of the polymer is integrated using Fixman's mid-point algorithm [23],

$$\begin{aligned} \boldsymbol{r}_i(t+\frac{\Delta t}{2}) &= \boldsymbol{r}_i(t) + \left(\boldsymbol{u}_i^0(t) + \sum_{j=0}^{N} \boldsymbol{\mu}_{ij}(t) \cdot \boldsymbol{F}_j^C(t) + \sum_{j=0}^{N} \boldsymbol{\mu}_{ij}(t) \cdot \boldsymbol{F}_j^B(t) \right) \Delta t \\ \boldsymbol{r}_i(t+\Delta t) &= \boldsymbol{r}_i(t) + \left(\boldsymbol{u}_i^0(t) + \sum_{j=0}^{N} \boldsymbol{\mu}_{ij}(t) \cdot \boldsymbol{F}_j^C(t) + \sum_{j=0}^{N} \boldsymbol{\mu}_{ij}(t+\frac{\Delta t}{2}) \cdot \boldsymbol{F}_j^B(t) \right) \Delta t, \end{aligned} \tag{12}$$

where $\boldsymbol{F}_j^B$ is a random force with co-variance

$$< \boldsymbol{F}_i^B \boldsymbol{F}_j^B >= 2T \boldsymbol{\mu}_{ij}^{-1} / \Delta t. \tag{13}$$

Here we use an Euler update of the drift velocity rather than a midpoint update [23], because, in conjunction with the excluded volume interaction, Eq. (3), and a bounded random number generator, the center of mass of the bead never crosses a wall. The upper bound, z_m, of the random number generator can be determined from the maximum bead displacement

$$\Delta y^{max} = \frac{2D_0 \Delta t}{y} - \sqrt{2 z_m D_0 \Delta t} > -y, \tag{14}$$

where the repulsive force for small y takes an approximate form $2T/y$ (ignoring the exponential term). The bead position remains positive provided $z_m \lesssim 4$, independent of the time-step, Δt; in our simulations $z_{m,BD} = 1$ and $z_{m,LB} = \sqrt{3}$. We use a similar time step as in our previous work, $\Delta t \approx 10^{-3} t_0$ [7].

III. RESULTS

The Weissenberg number, $\mathrm{Wi} = \gamma\tau$, characterizes the ambient flow-field and is defined as the product of a characteristic relaxation time of the polymer, τ, and the shear rate, γ. A linear polymer molecule in dilute solution has two distinct relaxation times: the viscous relaxation time, τ_σ, obtained from the autocorrelation of the polymer stress, σ_{xy}, and the longest conformational relaxation time, τ_1, obtained from the autocorrelation of the first normal mode, X_1, or the end-to-end vector, R_E. Within the Rouse and Zimm approximations, $\tau_1 = 2\tau_\sigma$. Single molecule experiments with DNA [24] suggest that τ_σ can be obtained by fitting the asymptotic decay of the maximum visible stretch, $\langle R_{max}(t) \rangle -$

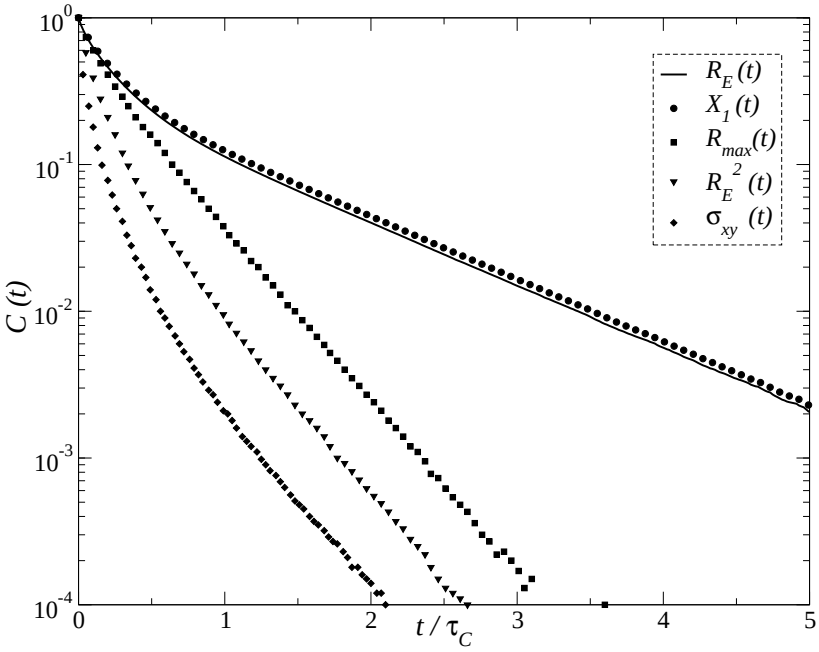

FIG. 2: Decay of the normalized correlation of $R_E(t)$, $X_1(t)$, $R_E^2(t)$, $R_{max}(t)$, and $\sigma_{xy}(t)$, Eq. (15). The slope of the linearly decaying regions are used to determine their relaxation times. Time t is made dimensionless using the Rouse relaxation time, τ_1.

$\langle R_{max}(\infty)\rangle$, to a single exponential. Here we take the maximum length of the polymer in the direction of its initial end-to-end vector as $R_{max}(t)$.

From BD simulations of a single polymer molecule at infinite dilution, we computed the normalized autocorrelation functions,

$$C(Z(t)) = \frac{\langle Z(t)Z(0)\rangle - \langle Z(\infty)\rangle^2}{\langle Z^2(0)\rangle - \langle Z(\infty)\rangle^2}, \tag{15}$$

where Z is one of the following polymer properties: X_1, R_E, R_E^2, R_{max} or σ_{xy}. The autocorrelation functions are obtained by averaging over a total time of approximately $10^8\tau_1$ using many different starting configurations of a fully equilibrated polymer molecule. The relaxation times shown in Table I are obtained by fitting the linear regions in Fig. 2 by a single exponential. Our results confirm that $\tau_1 \approx \tau_{R_E}$ and also that $\tau_{R_E^2} \approx \tau_\sigma \sim \tau_{R_{Max}}$, although the relaxation time from the maximum visible stretch deviates from the viscous relaxation time by almost 10%. The ratio of conformational to viscous relaxation times, $\tau_1 = 2.6\tau_\sigma$, differs from the Rouse and Zimm theories, primarily due to the excluded volume interaction. For an ideal harmonic chain $\tau_1 = 2\tau_\sigma$, but τ_1 can increase to $5\tau_\sigma$ when including excluded volume and finite extension [25]. In our present simulations, we take the viscous

Z	R_E	X_1	R_{max}	R_E^2	σ_{xy}
τ_Z	15.21	15.07	5.43	5.82	5.81

TABLE I: Relaxation times of a polymer chain from several different measures of the extension. The relaxation times are obtained by fitting the linear regions in Fig. 2 by a single exponential.

relaxation time $\tau_\sigma = 5.81t_0$ as the characteristic relaxation time defining the Weissenberg number, $\tau = \tau_\sigma$.

A. Uniform Shear Flow

The migration of a flexible polymer towards the center of the channel in response to a uniform shear flow is well-studied [6, 9, 12, 26]. The polymer chain stretches and orients itself in the presence of the local shear rate and the disturbance field reflected from a no-slip boundary then drives it away from the wall. The steady-state distribution of the polymer across the chann ystem.

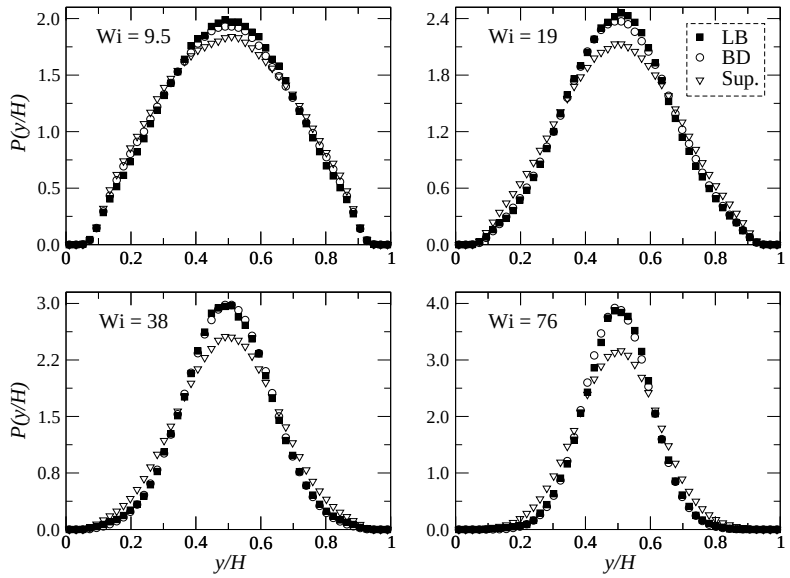

FIG. 3: Center of mass distribution of a confined polymer driven by uniform shear flow. Results for LB and BD simulations are compared for four values of the Weissenberg number, Wi $= \gamma\tau_\sigma$; the channel width is $H = 10R_G$

Figure 3 shows the center of mass distribution obtained from LB and BD simulations at four different values of the Weissenberg number. To obtain statistically precise data,

each profile is averaged over a time of approximately $1000\tau_H$; here $\tau_H = H^2/D = 3000t_0$ is the time required by the polymer chain to diffuse across the channel of width $H = 10R_G$, and $t_0 = 6\pi\eta a/\kappa$. Profiles from BD simulations were generated using both the superposed Green's function, Eq. (11), and the full Green's function, Eq. (10). The effect of multiple reflections is significant at higher shear rates; for instance at Wi = 76 the peak in the distribution is increased by 33% compared to the superposition approximation. Results from LB simulations at each Wi number show an identical depletion layer to the BD results obtained from the complete Green's function. The peaks of the distribution profile at all four Wi numbers are within 1% for the two simulation methods. The statistical uncertainties at each position are smaller than the size of the symbols.

The concentration profiles are insensitive to the choice of parameters used in the simulations. The LB data plotted in Fig. 3 used a time-step $\Delta t = 3 \times 10^{-3} t_0$, a periodic box length $L = 3H$, and a grid resolution $\Delta x = 2b$. Typically $\Delta x \leq b$ [5] is required to accurately capture hydrodynamic interactions within the polymer, but here a coarser grid resolution is sufficient to obtain the correct distribution of the center of mass, which is dominated by HI on the length scale of the polymer. Further reducing either the grid spacing or the time step produces no discernible effect on the concentration profile. We note that the LB and BD simulations use similar time steps, $\Delta t \sim 10^{-3} t_0$, despite the extra inertial time scale in the LB method.

The mean stretch of the polymer molecule is given by its end-to-end vector and the results obtained from the two methods for Wi = 9.5 are plotted in Fig. 4; comparisons at other Wi show similar trends. Results from LB simulations indicate a dependence on the effective time-step size, Δt, and the grid-resolution, Δx. By reducing the time-step $\Delta t/t_0$ from 5.9×10^{-3} to 1.5×10^{-3} (a fourfold increase in Sc) a convergent value for the mean polymer stretch in the center of the channel, $R_E^2 = 270b^2$ is obtained. Further reducing the effective time step produces no discernible change in R_E^2. A decrease in the grid spacing produced a further small reduction in R_E^2, from $270b^2$ to $259b^2$, close to the BD result, $R_E^2 = 250b^2$.

The results suggest that the mean end-to-end distance is a more sensitive measure of the disturbance in the flow-field than the distribution of the center of mass. In a shear flow, the polymer chain is stretched and the disturbance in the flow-field due to one bead has to travel a larger distance to affect the other beads. By decreasing the LB time-step,

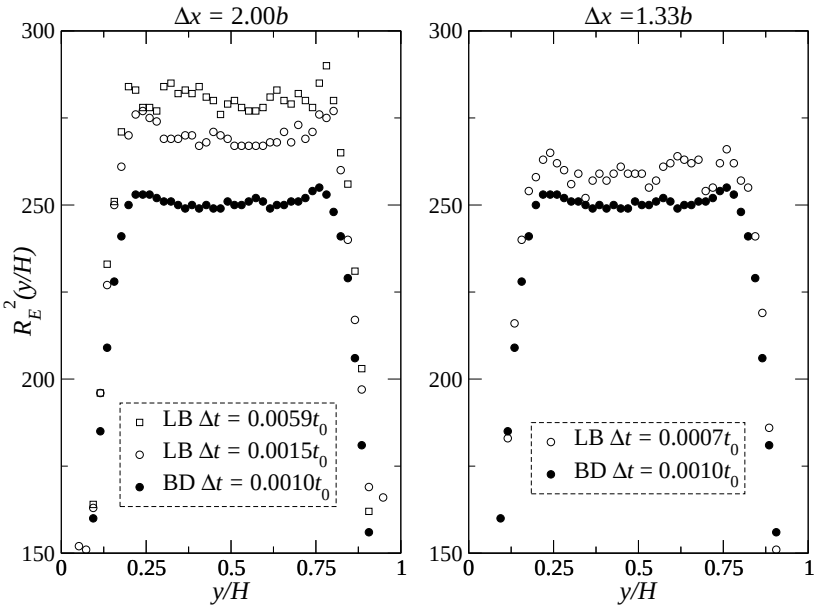

FIG. 4: Distribution of the end-to-end vector across the channel for a single confined polymer chain driven by uniform shear flow is compared for LB and BD simulations for Wi = 9.5. LB results are obtained for two values of grid resolution: $\Delta x/b = 2.00$ and 1.33 and three values of the time-step.

convergent results for the polymer stretch are obtained for each grid resolution. The results for the finer resolution, $\Delta x = 1.33b$, are within 2% of the BD results, similar to the results for an isolated chain with comparable grid resolution.

B. Pressure-driven Flow

A confined polymer chain in a pressure-driven flow also migrates away from the walls, but owing to the non-uniform shear rate, the preferred conformation of the molecule depends on its position in the channel. The diffusivity of the polymer chain and its migration velocity also vary with the distance from the no-slip boundaries. Close to the center of the channel the diffusivity of the polymer chain overcomes the transverse migration velocity [27], resulting in off-center peaks and a central dip in the polymer concentration profile. The distribution profiles from LB and BD are again in quantitative agreement, as shown in Fig. 5. The maximum deviations occur at Wi = 38; 3% at the off-center peaks and 4% at the central dip. At the highest Weissenberg number, Wi = 76, the flow-rate and temperature were reduced by a factor of 4 to eliminate an increased dependence on Δt. The higher Schmidt

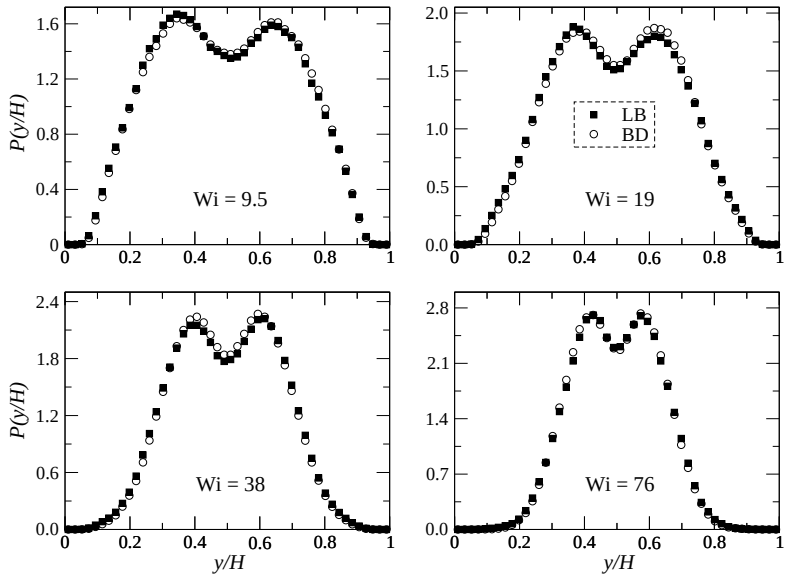

FIG. 5: Distribution of the center of mass for a confined polymer in a pressure-driven flow. Results for LB and BD simulations are compared for four values of the Weissenberg number, $\mathrm{Wi} = \gamma\tau_\sigma$.

number is apparently needed to allow the hydrodynamic interactions to propagate over the fully extended chain.

We do not have a satisfactory explanation for the discrepancies between LB and BD concentration profiles in pressure-driven flow shown in Fig. 4 of Ref. [14]. We note that the LB simulations in Ref. [14] neglected the thermal fluctuations in the fluid [4, 28], which means that the fluid-particle interactions corresponding to the correlated Brownian forces between beads are missing and only the single-particle Brownian force remains. We have attempted to replicate this mistake by turning off all the thermal fluctuations in the fluid, but at constant shear rate this leads to only quantitative differences in the concentration profiles and the dip in polymer concentration near the center of the channel remains. However, the neglect of thermal forces in the fluid also fails to satisfy the fluctuation-dissipation relation [28, 29] and leads to about a 70% overestimate of the polymer relaxation time [7]. Thus when comparing LB and BD simulations at constant Weissenberg numbers, the shear rate in the LB simulation will be too small by almost a factor of two; in other words a simulation at a nominal $\mathrm{Wi} = 100$ would actually be closer to $\mathrm{Wi} = 50$. Nevertheless, there should still be considerably more migration than shown in Fig. 4 of Ref. [14], and the distinctive double peak persists down to $\mathrm{Wi} < 10$ as can be seen in Fig. 5. Another possible source of disagreement is that Chen et al. used a dilute polymer solution in their LB

simulations rather than an isolated chain, presumably to improve the statistics. However, the low polymer concentration, $(4\pi/3)nR_g^3 = 0.02$ suggests that the chains are essentially independent, so the explanation for their results remains elusive. Nevertheless the results presented here show that LB does produce essentially identical results to Brownian dynamics, with careful control of the grid resolution and effective time step.

IV. CONCLUSIONS

Comparisons have been made between LB and BD simulations of a confined polymer chain driven by a uniform shear rate or pressure gradient. The center-of-mass distribution obtained from the two simulation methods is in quantitative agreement for all flow rates; this applies to both uniform shear and pressure-driven flows. A relatively coarse grid resolution, $\Delta x = 2b$, is sufficient to capture the effects of hydrodynamic interactions on the scale of the polymer, R_G. Our results do not agree with Fig. 4 of Ref. [14], which incorrectly suggest a qualitative disagreement between LB and BD simulations of a confined polymer in a pressure-driven flow.

Polymer extension is more sensitive to the small scale HI. The polymer is stretched by the shear, and the time taken for a disturbance in the flow-field to propagate to neighboring beads is larger. Convergent results for the polymer stretch require a two to four times smaller time-step than comparable simulations of a collapsed polymer. In addition a finer grid is needed to resolve the balance between the tension in the polymer, the shear, and the Brownian force. As Δx and Δt become small, convergent results are obtained for the polymer stretch as well.

Brownian dynamics simulations depend on an accurate Green's function for finite-size beads between two parallel plates. The mobility matrix computed using Eq. (10) is symmetric and positive-definite for all accessible configurations of the polymer. The superposed Green's function offers a computationally faster alternative for lower values of Wi; here the errors in the concentration profile are less than 5%. However, for $\mathrm{Wi} \geq 40$, the superposed solution is in error by more than 25% and reflections are necessary to properly account for the HI.

Acknowledgements

This work was supported by National Science Foundation grant No. CTS-0505929. The authors thank David Saintillan (University of Illinois) for providing a code for the two-wall Green's function.

APPENDIX A: PRETABULATING THE GREEN'S FUNCTION

Computing the mobility matrix of a pair of confined beads, Eq. (10), takes several orders of magnitude longer than the superposition approximation, Eq. (11). Thus, the contribution due to multiple reflections between the plates, $\mu^R_{ij,\alpha\beta} = \mathcal{L}_i\mathcal{L}_j G^R_{\alpha\beta}(\boldsymbol{r}_i, \boldsymbol{r}_j|H)$, is pretabulated and interpolated during the simulations; here the indexes i and j number the beads while α and β are the Cartesian components. The look-up table is constructed on a Cartesian grid with $N_y + 1$ grid points in the direction perpendicular to the wall (y) and $N_x + 1$ grid points in the directions parallel to the wall (x and z). The grid-spacings are $\Delta y = H/N_y$ and $\Delta x = \Delta z = L_C/N_x$ where L_C is the contour length of the polymer.

The mobility matrix, $\mu^R_{ij,\alpha\beta}$, is a function of the four dimensional vector $R_{ij} = [y_i, \boldsymbol{r}_{ij}]$, and each element in the look-up table can be identified by a set of four integer indexes, $\psi = (k_s, k_x, k_y, k_z)$:

$$R(\psi) = [k_s\Delta y, k_x\Delta x, k_y\Delta y, k_z\Delta x], \tag{A1}$$

where the domains of the indexes are

$$0 \le k_s \le N_y, \qquad -N_x \le k_x \le N_x, \qquad 0 \le k_y \le N_y, \qquad -N_x \le k_z \le N_x. \tag{A2}$$

The mobility matrix is interpolated from the elements of the look-up table,

$$\mu^R_{ij,\alpha\beta}(R_{ij}) = \sum_{\psi} \Delta(R_{ij} - R(\psi))\mu^R_{\alpha\beta}(R(\psi)), \tag{A3}$$

where $\Delta(R)$ is taken as the product of one-dimensional functions,

$$\Delta\left(R\left[y_s, x, y, z\right]\right) = \phi\left(\frac{y_s}{\Delta y}\right)\phi\left(\frac{x}{\Delta x}\right)\phi\left(\frac{y}{\Delta y}\right)\phi\left(\frac{z}{\Delta x}\right). \tag{A4}$$

We used linear interpolation

$$\phi(u) = \begin{cases} 1 - |u| & |u| \le 1, \\ 0 & |u| \ge 1. \end{cases} \tag{A5}$$

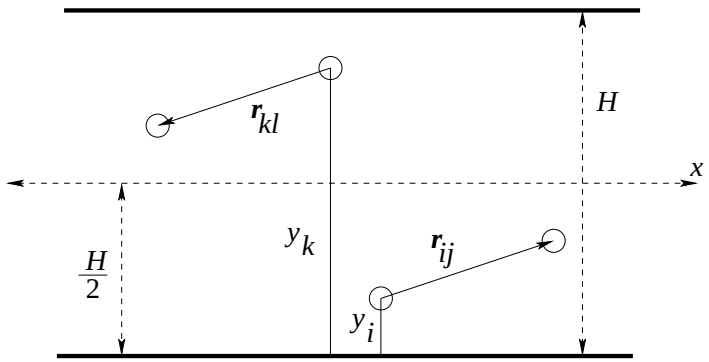

FIG. 6: Illustration of symmetry based on the center of the channel. The disturbance in the flow-field at $\boldsymbol{r}_{ij}$ relative to a source located at y_i is identical to the disturbance at $\boldsymbol{r}_{kl}$ relative to a source located at $y_k = H - y_i$.

The computational cost of constructing a look-up table with $(2N_x + 1)^2 \times (N_y + 1)^2$ elements can be significantly ($\approx 1/32$) reduced by exploiting the symmetries in $\mu^R_{ij,\alpha\beta}$. First, the symmetry of the mobility matrix is used,

$$\mu^R_{ij,\alpha\beta} = \mu^R_{ji,\beta\alpha}. \tag{A6}$$

Next, system-specific symmetries about the center of the channel and its axis perpendicular to the walls are used. The flow-field at $\boldsymbol{r}_j$ in Fig. 6, due to a source located at y_i is identical to the flow-field at $\boldsymbol{r}_l$ due to a source located at $y_k = H - y_i$, provided that $\boldsymbol{r}_{kl} = -\boldsymbol{r}_{ij}$. Thus,

$$\mu^R_{ij,\alpha\beta} = \mu^R_{kl,\alpha\beta}. \tag{A7}$$

Moreover, the confined system has cylindrical symmetry, as shown in Fig. 7. On a Cartesian grid there are eight equivalent locations indicated in the "Top View" of Fig. 7. The elements of the HI matrix at these locations can be obtained by swapping elements and signs:

$$\begin{gathered}
\mu^{R,2}_{ij,\alpha\beta} = \Upsilon_{\alpha\beta\gamma\delta}\ \mu^{R,1}_{ij,\gamma\delta} + (\Lambda_{\alpha\beta\gamma\delta} + \Lambda_{\delta\gamma\beta\alpha})\, \mu^{R,1}_{ij,\gamma\delta} \\
\mu^{R,3}_{ij,\alpha\beta} = \mu^{R,2}_{ij,\alpha\beta} - 2\,(A_{\alpha\beta\gamma\delta} + A_{\delta\gamma\beta\alpha})\, \mu^{R,2}_{ij,\gamma\delta}, \qquad \mu^{R,4}_{ij,\alpha\beta} = \mu^{R,1}_{ij,\alpha\beta} - 2\,(A_{\alpha\beta\gamma\delta} + A_{\delta\gamma\beta\alpha})\, \mu^{R,1}_{ij,\gamma\delta} \\
\mu^{R,5}_{ij,\alpha\beta} = \mu^{R,1}_{ij,\alpha\beta} - 2\,(B_{\alpha\beta\gamma\delta} + B_{\delta\gamma\beta\alpha})\, \mu^{R,1}_{ij,\gamma\delta}, \qquad \mu^{R,6}_{ij,\alpha\beta} = \mu^{R,2}_{ij,\alpha\beta} - 2\,(B_{\alpha\beta\gamma\delta} + B_{\delta\gamma\beta\alpha})\, \mu^{R,2}_{ij,\gamma\delta} \\
\mu^{R,7}_{ij,\alpha\beta} = \mu^{R,2}_{ij,\alpha\beta} - 2\,(C_{\alpha\beta\gamma\delta} + C_{\delta\gamma\beta\alpha})\, \mu^{R,2}_{ij,\gamma\delta}, \qquad \mu^{R,8}_{ij,\alpha\beta} = \mu^{R,1}_{ij,\alpha\beta} - 2\,(C_{\alpha\beta\gamma\delta} + C_{\delta\gamma\beta\alpha})\, \mu^{R,1}_{ij,\gamma\delta}
\end{gathered} \tag{A8}$$

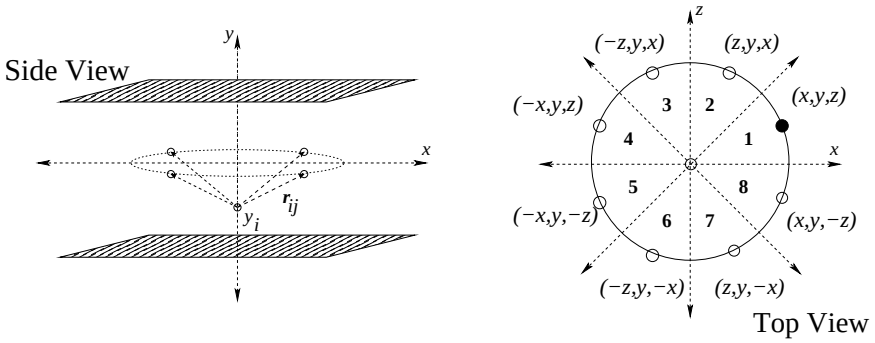

FIG. 7: Illustration of cylindrical symmetry in the system. The source bead is located at y_i. The disturbance field at the receiver (solid line in top view) is related to the indicated locations (dashed lines) through simple linear operations given by Eqs. (A8) and (A9).

where Υ, Λ, A, B, and C are fourth-rank tensors,

$$\begin{aligned}
\Upsilon_{\alpha\beta\gamma\delta} &= \delta_{\alpha x}\delta_{\beta z}\delta_{\gamma x}\delta_{\delta z} + \delta_{\alpha y}\delta_{\beta y}\delta_{\gamma y}\delta_{\delta y} + \delta_{\alpha z}\delta_{\beta x}\delta_{\gamma z}\delta_{\delta x}, \\
\Lambda_{\alpha\beta\gamma\delta} &= \delta_{\alpha z}\delta_{\beta z}\delta_{\gamma x}\delta_{\delta x} + \delta_{\alpha y}\delta_{\beta z}\delta_{\gamma y}\delta_{\delta x} + \delta_{\alpha z}\delta_{\beta y}\delta_{\gamma x}\delta_{\delta y}, \\
A_{\alpha\beta\gamma\delta} &= \delta_{\alpha x}\delta_{\beta y}\delta_{\gamma x}\delta_{\delta y} + \delta_{\alpha x}\delta_{\beta z}\delta_{\gamma x}\delta_{\delta z}, \\
B_{\alpha\beta\gamma\delta} &= \delta_{\alpha x}\delta_{\beta y}\delta_{\gamma x}\delta_{\delta y} + \delta_{\alpha y}\delta_{\beta z}\delta_{\gamma y}\delta_{\delta z}, \\
C_{\alpha\beta\gamma\delta} &= \delta_{\alpha y}\delta_{\beta z}\delta_{\gamma y}\delta_{\delta z} + \delta_{\alpha z}\delta_{\beta x}\delta_{\gamma z}\delta_{\delta x}.
\end{aligned} \tag{A9}$$

The limits on the indexes of the reduced look-up table are,

$$0 \le k_s \le \lceil N_y/2 \rceil, \quad 0 \le k_x \le N_x, \quad k_s \le k_y \le N_y, \quad k_x \le k_z \le N_x. \tag{A10}$$

A grid with $N_y = 25$ and $N_x = 15$ generates convergent migration profiles for all the cases reported in this paper. A sparser grid (or $\Delta x \gg \Delta y$) can be used in the direction parallel to the wall because the polymer is extended in that direction by the shear.

[1] B. Dünweg and A. J. C. Ladd, Adv. Polym. Sci. **221**, 89 (2009).

[2] R. D. Groot and P. B. Warren, J. Chem. Phys. **107**, 4423 (1997).

[3] G. Gompper, T. Ihle, D. M. Kroll, and R. G. Winkler, Advan. Polym. Sci. **221**, 1 (2009).

[4] A. J. C. Ladd, J. Fluid Mech. **271**, 285 (1994).

[5] P. Ahlrichs and B. Dünweg, J. Chem. Phys. **111**, 8225 (1999).

[6] O. B. Usta, A. J. C. Ladd, and J. E. Butler, J. Chem. Phys. **122**, 094902 (2005).

[7] A. J. C. Ladd, R. Kekre, and J. E. Butler, Phys. Rev. E **80**, 036704 (2009).

[8] T. T. Pham, U. D. Schiller, J. R. Prakash, and B. Dünweg, J. Chem. Phys. **131**, 16 (2009).

[9] R. M. Jendrejack, D. C. Schwartz, J. J. de Pablo, and M. D. Graham, J. Chem. Phys. **120**, 2513 (2004).

[10] R. Khare, M. D. Graham, and J. J. de Pablo, Phys. Rev. Lett. **96**, 224505 (2006).

[11] J. Park, J. M. Bricker, and J. E. Butler, Phys. Rev. E **76**, 040801 (2007).

[12] L. Fang, H. Hu, and R. G. Larson, J. Rheol. **49**, 127 (2005).

[13] D. Stein, F. H. J. van der Heyden, W. J. A. Koopmans, and C. Dekker, Proc. Natl. Acad. Sci. U. S. A. **103**, 15853 (2006).

[14] Y. L. Chen, H. Ma, M. D. Graham, and J. J. de Pablo, Macromolecules **40**, 5978 (2007).

[15] J. W. Swan and J. F. Brady, Phys. Fluids **19**, 13306 (2007).

[16] N. Liron and S. Mochon, J. Eng. Math. **10**, 287 (1976).

[17] R. M. Jendrejack, M. D. Graham, and J. dePablo, J. Chem. Phys **113**, 2894 (2000).

[18] R. M. Jendrejack, J. J. de Pablo, and M. D. Graham, J. Chem. Phys. **116**, 7752 (2002).

[19] J. R. Blake, Proc. Camb. Phil. Soc. **70**, 303 (1971).

[20] J. Rotne and S. Prager, J. Chem. Phys. **50**, 4831 (1969).

[21] M. E. Staben, A. Z. Zinchenko, and R. H. Davis, Phys. Fluids **15**, 1711 (2003).

[22] M. E. Staben, A. Z. Zinchenko, and R. H. Davis, Phys. Fluids **16**, 4206 (2004).

[23] M. Fixman, J. Chem. Phys. **69**, 1538 (1978).

[24] T. T. Perkins, D. E. Smith, and S. Chu, Science **276**, 2016 (1997).

[25] J. G. H. Cifre, R. Pamies, M. C. L. Martinez, and J. G. de la Torre, J. Non-Cryst. Solids **352**, 5081 (2006).

[26] H. Ma and M. D. Graham, Phys. Fluids. **17**, 083103 (2005).

[27] M. S. Jhon and K. F. Freed, J.Polym. Sci.Part B **23**, 955 (1985).

[28] R. Adhikari, K. Stratford, M. E. Cates, and A. J. Wagner, Europhys. Lett. **71**, 473 (2005).

[29] B. Dünweg, U. D. Schiller, and A. J. C. Ladd, Phys. Rev. E **76**, 036704 (2007).